Quantitative analyses of enhanced thermoelectric properties of modulation-doped PEDOT:PSS/ undoped Si (001) nanoscale heterostructures

Citation: Lee, Dongwook, et al. "Quantitative Analyses of Enhanced Thermoelectric Properties of Modulation-Doped PEDOT:PSS/undoped Si (001) Nanoscale Heterostructures." Nanoscale 8, 47 (November 2016): 19754–19760 © 2016 The Royal Society of Chemistry

As Published: http://dx.doi.org/10.1039/c6nr06950a

Publisher: Royal Society of Chemistry

Persistent URL: http://hdl.handle.net/1721.1/112327

Version: Author's final manuscript: final author's manuscript post peer review, without publisher's formatting or copy editing

Nanoscale

ARTICLE

Quantitative Analyses of Enhanced Thermoelectric Properties of Modulation-Doped PEDOT:PSS / Undoped Si (001) Nanoscale Heterostructures

Received 00th January 20xx,
Accepted 00th January 20xx

DOI: 10.1039/x0xx00000x

www.rsc.org/nanoscale

Dongwook Lee[a], Sayed Youssef Sayed[b, ¶, ‡], Sangyeop Lee[c, ‡], Chris Adam Kuryak[c], Jiawei Zhou[c], Gang Chen[c, *], and Yang Shao-Horn[a, b, c, *]

Poly(3,4-ethylenedioxythiophene) poly(styrenesulfonate) (PEDOT:PSS) has high electrical conductivity (~ 10^3 S/cm) but exhibits low Seebeck coefficient (< 15 μV/K), resulting in low power factor. Mixing PEDOT:PSS with nanostructured semiconductors can enhance Seebeck coefficient and achieve improved thermoelectric power factor. However, underlying mechanisms for those composite thermoelectric systems are scarcely understood so far. In this study, quantitative analyses on electrical conductivity and Seebeck coefficient for the heterostructures of nanometer-thick PEDOT:PSS on single-crystal Si (001) on sapphire (SOS) are reported. The heterostructures have larger Seebeck coefficients up to 7.3 fold and power factors up to 17.5 fold relative to PEDOT:PSS. Electrical conductivity increased with decreasing combined thicknesses of PEDOT:PSS and Si, and Seebeck coefficient increased with decreasing PEDOT:PSS thickness, which can be attributed to modulation doping caused by diffusion of holes from PEDOT:PSS into undoped Si. This hypothesis is supported by simulation per band alignment. The valence band offset between Si and PEDOT:PSS dominantly controls electrical conductivity and Seebeck coefficient of the heterostructures. This study not only suggests mechanistic insights to increase the power factors of PEDOT:PSS-based composites but also opens the door for new strategies to enhance the thermoelectric efficiencies of heterostructured nanocomposite materials.

1. Introduction

Thermoelectric devices convert wasted heat into electrical energy[1, 2]. However, current thermoelectric devices can only achieve less than 15% of energy efficiency[3]. Much research has aimed at increasing the device efficiency by increasing dimensionless figure of merit of thermoelectric materials[4, 5], which is described $ZT = \frac{\sigma S^2}{\kappa}$, where S, σ, and κ represent Seebeck coefficient, electrical conductivity, and thermal conductivity, respectively[2]. State-of-the-art thermoelectric materials such as $Bi_2(Te_{1-x}Se_x)_3$ alloys have power factors ($S^2\sigma$) of up to 5500 μW/K²·m and ZT near unity[2, 6]. However, these alloys are expensive, difficult to process and toxic. An alternative approach is to employ organic semiconductors such as conducting polymers as they are inexpensive and easy to process[7]. Conducting polymers such as polypyrrole[8] and perylene-3,4,9,10-tetracarboxylicdianhydride (PTCDA)[9] have comparable electrical conductivities (10^{-2} ~ 10^3 S/cm[8, 9]) to inorganic thermoelectric materials (up to 3200 S/cm for $Bi_2(Te_{1-x}Se_x)_3$ alloys[6]) but significantly lower Seebeck coefficients (< 15 μV/K), which renders power factors up to 22.5 μW/m·K², two orders of magnitude lower than those of $Bi_2(Te_{1-x}Se_x)_3$ alloys[2, 6].

Recently, tuning the hole density in PEDOT:PSS[10-13] has been shown to enhance the power factor of PEDOT:PSS reaching a power factor of 480 μW/m·K², which makes PEDOT:PSS a promising material to explore for thermoelectric applications. In addition, mixing PEDOT:PSS with inorganic thermoelectric materials such as Te nanowires[14, 15], and Bi_2Te_3 nanostructures[16, 17], and carbon-based nanostructures[18] including graphene[19], has led to enhanced power factors of varying degrees for the composites. The physical origin for the enhanced power factor in these composites has been attributed to energy dependent charge carrier scattering[15, 16, 20-23] and modulation doping [15, 16, 24-31]. Charge carrier filtering[15, 16, 20-23] (Figure 1a – 1b) assumes that the electrons with low energy are more scattered compared to the electrons with high energy, sharpening the effective density of states of the composites, thereby elevating the Seebeck coefficient at the expense of electrical conductivity due to fewer carriers for electrical conduction[24-27, 28-31]. When charge carriers encounter an interface, lower energy carriers are scattered more, leading to higher Seebeck coefficient at the expense of reduced

[a] Department of Materials Science and Engineering, Massachusetts Institute of Technology, Cambridge, Massachusetts, United States, 02139
[b] The Research Laboratory of Electronics, Massachusetts Institute of Technology, Cambridge, Massachusetts, United States, 02139
[c] Department of Mechanical Engineering, Massachusetts Institute of Technology, Cambridge, Massachusetts, United States, 02139

† Electronic Supplementary Information (ESI) available. See DOI: 10.1039/x0xx00000x

‡ These authors contributed equally.

¶ Permanent address: Department of Chemistry, Faculty of Science, Cairo University, Giza, 12613, Egypt.

electrical conductivity[21, 23]. However, previous research has shown the electrical conductivity and Seebeck coefficient of composites can increase simultaneously, from 1.32 S/cm and 18.9 μV/K of PEDOT:PSS to 19.3 S/cm and 163 μV/K of the PEDOT:PSS / Te nanowires composite[15], which does not match with the concept of charge carrier filtering. In addition, modulation doping (Figure 1c – 1d), where charge carriers in a more doped material migrate to adjacent and less doped materials with higher mobility[28-31], can increase the electrical conductivity without sacrificing conductive charge carrier density compared to directly doping the material due to reduced ionized impurity scattering. This strategy has been applied to enhance power factor of Si_xGe_{1-x} alloy composite system with nanoparticles embedded in matrix, where more doped Si or $Si_{70}Ge_{30}$ nanoparticles provided charge carriers to less doped $Si_{80}Ge_{20}$ or $Si_{95}Ge_5$ matrix, rendering higher mobility without decreasing the Seebeck coefficient[29, 30]. As a degenerate p-type semiconductor, PEDOT:PSS can function as a modulation-dopant to an undoped semiconductor pair, even though this possibility has never been explored before.

In this work, we employ model heterostructures of nanometer-thick PEDOT:PSS deposited on single-crystal Si (001) on sapphire (SOS) to study how the electrical conductivity and Seebeck coefficient change as a function of PEDOT:PSS thickness. Undoped Si (001) was selected due to its well-known surface chemistry and band structure, and high Seebeck coefficients such as 1.3 mV/K at 10^{14} cm^{-3} of undoped hole density[32-35]. Six Si thicknesses of SOS (14 nm, 41 nm, 46 nm, 59 nm, 100 nm, and 250 nm) were used and PEDOT:PSS thickness varied from 5 nm to 60 nm. Such heterostructures were found to enhance the Seebeck coefficient and the power factor from those of PEDOT:PSS.

2. Experimental

Single-crystal silicon (001) on sapphire (SOS) (Precision Micro-Optics) was first cut into 1.0 × 1.0 cm^2 by dicing saw, which was washed by acetone (Sigma Aldrich, 270725, ≥ 99.9 %), isopropanol (Sigma Aldrich, I9030, > 99.0%) and then deionized water (18.2 MΩ·cm). The SOS was immersed subsequently in 1:3 volumetric mixture of hydrogen peroxide (Sigma Aldrich, 349887, 35 wt% aqueous solution) and sulfuric acid (Sigma Aldrich, 258105, 95 – 98 %) for 10 minutes to remove surface organic species, which was followed by etching in diluted 4.8 wt% hydrofluoric acid (Sigma Aldrich, 695068, 48 %) for 3 minutes to remove the native oxide. Further oxidation of the etched Si surface was performed with 10 vol% piranha aqueous solution for 5 minutes in order to accommodate the hydrophilicity of PEDOT dispersion and control the morphologies of PEDOT:PSS on Si (001). Water-dispersed, PEDOT:PSS (Clevios PH1000) was mixed to dimethyl sulfoxide (DMSO, Sigma Aldrich, D8418) with 20 to 1 mass ratio by ultrasonication for 15 minutes, which was shown to provide high electrical conductivities up to ~ 10^2 S/cm[36-39]. The second step involves adding 5 parts of ethanol (200 Proof, Koptec) to 1 part of the polymer dispersion by volume, which was homogenized with horn-ultrasonicator for 5 minutes in order to increase the wettability and thus surface uniformity of PEDOT:PSS films on Si (001). PEDOT:PSS dispersion of 50 μL was spin-coated on SOS at 2000 RPM with 180 seconds of dwell time. PEDOT:PSS thickness was further grown by repeating the spin-coating under the same condition mentioned earlier.

3. Results and discussion

Atomic force microscopy (AFM) was used to reveal and monitor the morphologies of PEDOT:PSS on SOS, which was compared with that of 10-nm-thick PEDOT:PSS deposited on hydrophilic SiO_2 glass substrate (VWR, 48366-045) as reference, with RMS roughness of 1.48 nm in Figure 2a. The Si (001) of SOS following the hydrofluoric acid etching was hydrophobic and the deposition of PEDOT:PSS was not uniform (Figure 2d), which exhibited a markedly different morphology from that found on SiO_2 glass, suggesting that PEDOT:PSS on HF-treated Si may not intact. This is further supported by electrical resistivity of the sample represented in Figure 2d is the same as that of bare SOS (4.6×10^3 Ω·cm). In contrast, PEDOT:PSS deposited on the Si (001) following the piranha treatment and 10 vol% diluted piranha treatment (with RMS roughness of 1.51 nm and 1.44 nm in Figure 2b - 2c) was found to have similar morphologies to that on SiO_2 glass, which were attributed to the formation of subnanometer SiO_x as revealed by X-ray reflectivity measurements (see Figure S2 in the ESI†). Therefore, the electrical conductivity and Seebeck coefficient measurements were made on the Si (001) following the 10 vol% diluted piranha.

Having PEDOT:PSS thicknesses smaller than 80 nm, the electrical conductivities of PEDOT:PSS/Si heterostructures were found to increase while the Seebeck coefficient decreases with increasing PEDOT:PSS thickness at six different Si thicknesses, as shown in Figure 3. The electrical conductivity of the heterostructure was obtained by normalizing the sheet conductance (decreasing with the combined thickness of PEDOT:PSS and Si shown in Figure S6 in the ESI†) by the combined thickness:

$$\bar{\sigma} = \frac{1}{R(d_1+d_2)} \quad (1)$$

where d_1 and d_2 represent the thickness of Si and PEDOT:PSS, respectively, and R represents the sheet resistance. The electrical conductivity of the heterostructure was higher at smaller thicknesses of Si in SOS for a given PEDOT:PSS thickness, as a consequence of the normalization. The y-intercepts of the electrical conductivity values in Figure 3 are positive, but close to 0, indicating only small contribution from the PEDOT:PSS / Si interfacial region to overall electrical conductivity. However, contribution of Si to overall Seebeck coefficient is not small, as will be shown below.

The Seebeck coefficient of the heterostructure was found to markedly increase with decreasing PEDOT:PSS thickness, reaching 80 μV/K at 6.5 nm of PEDOT:PSS thickness, which is considerably higher than that of PEDOT:PSS. On the other hand, unlike the electrical conductivity trends, no noticeable

changes were found for the Seebeck coefficient as a function of Si thickness. It is proposed that the increasing Seebeck coefficient with decreasing PEDOT:PSS thickness can be attributed to modulation doping at the PEDOT:PSS / Si interface.

The influence of modulation doping on the electrical conductivity and Seebeck coefficient was numerically assessed using Poisson's equation, where equilibrium band alignment and band bending around the interface was taken into account. Since the transport parameters[36, 40, 41] and work function[42-44] of PEDOT:PSS are highly dependent on the sample preparation, the work function of a representative PEDOT:PSS sample deposited on SiO_2 glass was measured using ultraviolet photoemission spectroscopy (UPS), as shown in Figure 4a. By reading the x-intercept of spectra, the work function was estimated as 5.03 eV. Valence band offset of Si and PEDOT:PSS, as well as the initial Fermi level of the Si determines the charge transfer direction and degree of modulation doping and therefore Seebeck coefficient. Energy levels before Si and PEDOT:PSS are in contact are shown in Figure 4b. According to Anderson's rule[45], the valence band edge offset can be determined. Upon contact, electrons will transfer from the higher Fermi level material to lower Fermi level side, eventually leading to the alignment of Fermi level on both sides (Figure 4c). For Si and PEDOT:PSS interface, this means holes transfer from the PEDOT:PSS side to the Si side, consistent with experimental data. Using the electron affinity and band gap of Si and PEDOT:PSS, the valence band edge offset was determined to be 0.111 eV. The simulated band bending at the interface of PEDOT:PSS / Si is shown in Figure 4c. PEDOT:PSS was found to have no band bending in the valence band due to its high hole density while the valence band of Si near the interface shows upward band bending, which results in higher hole density in Si close to the interface. The measured electrical conductivity of PEDOT:PSS, measured work function and other inputs used for Poisson's equation were summarized in Table 1.

The influence of modulation doping by band bending on the electrical conductivity and Seebeck coefficient was further examined. The simulated electrical conductivity and Seebeck coefficient of heterostructures associated with band bending (unbroken lines in Figure 3) were obtained by the following formulas, assuming parallel resistors model[46, 47]:

$$\bar{\sigma}(d_1, d_2) = \frac{e\int_{-d_1}^{d_2} n(x)\mu(x)dx}{d_1+d_2} \quad (2)$$

$$\bar{S}(d_1, d_2) = \frac{e\int_{-d_1}^{d_2} n(x)\mu(x)S(x)dx}{\bar{\sigma}(d_1,d_2)\cdot(d_1+d_2)} \quad (3)$$

where $n(x)$, $\mu(x)$, and $S(x)$ are hole density, mobility, and Seebeck coefficient of each position x in the PEDOT:PSS / Si heterostructure. When no band bending is assumed at the PEDOT:PSS / Si interface (dashed lines in Figure 3), the electrical conductivity and Seebeck coefficient of the heterostructures were estimated by following formulas:

$$\bar{\sigma}(d_1, d_2) = \frac{\sigma_1 d_1+\sigma_2(d_2)d_2}{d_1+d_2} \quad (4)$$

$$\bar{S}(d_1, d_2) = \frac{S_1\sigma_1 d_1+S_2\sigma_2(d_2)d_2}{\bar{\sigma}(d_1,d_2)\cdot(d_1+d_2)} \quad (5)$$

where S_1, σ_1, and S_2, are Seebeck coefficient and electrical conductivity of Si, and Seebeck coefficient of PEDOT:PSS respectively, and kept constants per no band bending assumption. However, $\sigma_2(d_2)$, electrical conductivity of PEDOT:PSS turned out to be a function of its thickness, even on completely non-semiconducting SiO_2 quartz substrate (Figure S7 in the ESI†), hence this effect was taken into account. Simulated electrical conductivities regardless of assuming band bending agree well with experimental measurements (Figure 3), which is in agreement with the lack of band bending in the PEDOT:PSS layer in Figure 4c. Band alignment simulation of the heterostructures with different Si thicknesses consistently shows that transferred holes from PEDOT:PSS into Si mainly stay at the interface (Figure 4c and Figure S10 in the ESI†). As the hole population in undoped Si is typically 6 orders of magnitude smaller than that of PEDOT:PSS[38, 48], it only minutely contributes to the overall electrical conductivity despite the 4 orders of magnitude higher mobility of Si[38, 40, 48, 49]. Therefore, the electrical conductivity rises as thickness of Si decreases as noncontributing Si far from the interface is removed from the electrical conductivity estimation, as seen in Figure 3. The slight upshift in the electrical conductivity from without band bending to with band bending (dotted blue lines and unbroken blue lines in Figure 3) is a consequence of hole injection from PEDOT:PSS to Si, which elevates the electrical conductivity of Si adjacent to the interface. Although the comparison of electrical conductivity through experiment and simulation validates the parallel resistor model, clearly, the electrical conductivity trends alone could not provide evidence in support of proposed modulation doping at the PEDOT:PSS / Si interface.

However, the simulated Seebeck coefficients associated with band bending agree with the experimentally observed enhancement in the Seebeck coefficient with decreasing PEDOT:PSS thickness. In contrast, no increase for the simulated Seebeck coefficient of the heterostructures (black dashed lines in Figure 3) was found with decreasing PEDOT:PSS thickness when the band bending was not considered. Therefore, combined experimental and simulated results in Figure 3 support that band bending driven modulation doping is responsible for the enhancement in Seebeck coefficient. Furthermore, when PEDOT:PSS thickness is less than 10 nm, the Seebeck coefficient changes rapidly, because influence of PEDOT:PSS with small Seebeck coefficient quickly overwhelms Seebeck coefficient of modulation-doped Si by its much higher electrical conductivity. Seebeck coefficient trends do not vary upon different Si thicknesses down to 14 nm, and this indicates modulation doping only happens close to the interface.

A maximum power factor was achieved in the heterostructure with the smallest PEDOT:PSS and Si thickness: 6.5 nm thick PEDOT:PSS on 14 nm thick Si, as shown in Fig S12. The Seebeck coefficient was increased from 10 μV/K of PEDOT:PSS on SiO_2 glass to 73 μV/K of the heterostructure, and the power factor was increased from 1.5 μW/m·K² to 26.2 μW/m·K², as shown in Figure 5.

Conclusions

In this work, we quantitatively demonstrated that modulation doping at the interface between PEDOT:PSS and Si heterostructure can lead to enhanced Seebeck coefficients and power factor by showing the agreement between the experimental results and simulated thermoelectric properties. Decreasing thickness of PEDOT:PSS can increase the Seebeck coefficient in the expense of electrical conductivity. The power factor was maximized when the thicknesses of both PEDOT:PSS and Si were at their minimum, because Seebeck coefficient is more critical to the power factor than electrical conductivity. Simulated electrical conductivity data with and without equilibrated PEDOT:PSS / Si interfacial band structure agree with experimental electrical conductivities, as the conduction by the modulation doped Si concentrated at the interface only contributes in small portion to the overall electrical conductivity. Simulated Seebeck coefficients obtained from equilibrated PEDOT:PSS / Si interface match well with the experimentally measured Seebeck coefficient, indicating that hole migration to Si is responsible for the enhancement of the Seebeck coefficient. Such information provides mechanistic insights into strategies to increase the power factor of PEDOT:PSS-based composites for thermoelectric applications. Future studies are needed to further explore band alignments and the magnitude of charge transfer at the interface in order to take advantage of the high Seebeck coefficient and mobility from the inorganic semiconductor to enhance the power factor of heterostructure materials.

Acknowledgements

We acknowledge the financial support of the Solid State Solar-Thermal Energy Conversion Center (S^3TEC), an Energy Frontier Research Center funded by the U.S. Department of Energy, Office of Basic Energy Sciences under Award No. DE-SC0001299. Dongwook Lee and Sangyeop Lee appreciate financial support by Samsung Scholarship. Sayed Youssef Sayed was supported by supported in part by the Skoltech-MIT Center for Electrochemical Energy Storage. Sayed Youssef Sayed also acknowledges the support of a postdoctoral fellowship from the Natural Sciences and Engineering Research Council (NSERC) of Canada. This work was performed in part at the Center for Nanoscale Systems (CNS), a member of the National Nanotechnology Infrastructure Network (NNIN), which is supported by the National Science Foundation under NSF award no. ECS-0335765. CNS is part of Harvard University. We also would like to appreciate Dr. Dimitre Karpuzov at University of Alberta for his UPS measurements.

Notes

† Electronic Supplementary Information (ESI) available. See DOI: 10.1039/x0xx00000x

‡ These authors contributed equally.

References

1 A. Majumdar, *Nat Nano*, 2009, **4**, 214-215.
2 G. J. Snyder and E. S. Toberer, *Nat Mater*, 2008, **7**, 105-114.
3 S. LeBlanc, S. K. Yee, M. L. Scullin, C. Dames and K. E. Goodson, *Renewable and Sustainable Energy Reviews*, 2014, **32**, 313-327.
4 M. S. Dresselhaus, G. Chen, M. Y. Tang, R. G. Yang, H. Lee, D. Z. Wang, Z. F. Ren, J. P. Fleurial and P. Gogna, *Advanced Materials*, 2007, **19**, 1043-1053.
5 M. Zebarjadi, K. Esfarjani, M. S. Dresselhaus, Z. F. Ren and G. Chen, *Energy Environ. Sci.*, 2012, **5**, 5147-5162.
6 S. Wang, G. Tan, W. Xie, G. Zheng, H. Li, J. Yang and X. Tang, *Journal of Materials Chemistry*, 2012, **22**, 20943-20951.
7 Z. Bao, *Nat Mater*, 2004, **3**, 137-138.
8 N. T. Kemp, A. B. Kaiser, C. J. Liu, B. Chapman, O. Mercier, A. M. Carr, H. J. Trodahl, R. G. Buckley, A. C. Partridge, J. Y. Lee, C. Y. Kim, A. Bartl, L. Dunsch, W. T. Smith and J. S. Shapiro, *Journal of Polymer Science Part B: Polymer Physics*, 1999, **37**, 953-960.
9 J. Wuesten, C. Ziegler and T. Ertl, *Physical Review B*, 2006, **74**.
10 G. H. Kim, L. Shao, K. Zhang and K. P. Pipe, *Nat Mater*, 2013, **12**, 719-723.
11 O. Bubnova, Z. U. Khan, A. Malti, S. Braun, M. Fahlman, M. Berggren and X. Crispin, *Nat Mater*, 2011, **10**, 429-433.
12 O. Bubnova, M. Berggren and X. Crispin, *Journal of the American Chemical Society*, 2012, **134**, 16456-16459.
13 T. Park, C. Park, B. Kim, H. Shin and E. Kim, *Energy & Environmental Science*, 2013, **6**, 788.
14 S. K. Yee, N. E. Coates, A. Majumdar, J. J. Urban and R. A. Segalman, *Physical chemistry chemical physics : PCCP*, 2013, **15**, 4024-4032.
15 K. C. See, J. P. Feser, C. E. Chen, A. Majumdar, J. J. Urban and R. A. Segalman, *Nano letters*, 2010, **10**, 4664-4667.
16 Y. Du, K. F. Cai, S. Chen, P. Cizek and T. Lin, *ACS Appl Mater Interfaces*, 2014, **6**, 5735-5743.
17 B. Zhang, J. Sun, H. E. Katz, F. Fang and R. L. Opila, *ACS applied materials & interfaces*, 2010, **2**, 3170-3178.
18 C. Gao and G. Chen, *Composites Science and Technology*, 2016, **124**, 52-70.
19 K. Xu, G. Chen and D. Qiu, *Journal of Materials Chemistry A*, 2013, **1**, 12395-12399.
20 A. Shakouri, *Annual Review of Materials Research*, 2011, **41**, 399-431.
21 D. Vashaee and A. Shakouri, *Physical Review Letters*, 2004, **92**, 106103.
22 A. Shakouri, C. LaBounty, P. Abraham, J. Piprek and J. E. Bowers, *MRS Online Proceedings Library Archive*, 1998, **545**, 449 (410 pages).
23 D. Vashaee and A. Shakouri, *Journal of Applied Physics*, 2004, **95**, 1233-1245.
24 J. M. O. Zide, D. Vashaee, Z. X. Bian, G. Zeng, J. E. Bowers, A. Shakouri and A. C. Gossard, *Physical Review B*, 2006, **74**.
25 A. J. Minnich, H. Lee, X. W. Wang, G. Joshi, M. S. Dresselhaus, Z. F. Ren, G. Chen and D. Vashaee, *Physical Review B*, 2009, **80**.
26 D. Vashaee and A. Shakouri, *Physical Review Letters*, 2004, **92**.
27 P. Jha, T. D. Sands, L. Cassels, P. Jackson, T. Favaloro, B. Kirk, J. Zide, X. Xu and A. Shakouri, *Journal of Applied Physics*, 2012, **112**, 063714.
28 R. Dingle, H. L. Störmer, A. C. Gossard and W. Wiegmann, *Applied Physics Letters*, 1978, **33**, 665-667.
29 B. Yu, M. Zebarjadi, H. Wang, K. Lukas, D. Wang, C. Opeil, M. Dresselhaus, G. Chen and Z. Ren, *Nano letters*, 2012, **12**, 2077-2082.

30 M. Zebarjadi, G. Joshi, G. Zhu, B. Yu, A. Minnich, Y. Lan, X. Wang, M. Dresselhaus, Z. Ren and G. Chen, *Nano Lett*, 2011, **11**, 2225-2230.
31 J. L. Boland, S. Conesa-Boj, P. Parkinson, G. Tütüncüoglu, F. Matteini, D. Rüffer, A. Casadei, F. Amaduzzi, F. Jabeen, C. L. Davies, H. J. Joyce, L. M. Herz, A. Fontcuberta i Morral and M. B. Johnston, *Nano Lett*, 2015, **15**, 1336-1342.
32 B. Lee, K. Kim, S. Lee, J. H. Kim, D. S. Lim, O. Kwon and J. S. Lee, *Nano Lett*, 2012, **12**, 4472-4476.
33 H.-K. Lyeo, A. A. Khajetoorians, L. Shi, K. P. Pipe, R. J. Ram, A. Shakouri and C. K. Shih, *Science*, 2004, **303**, 816-818.
34 Z. Bian, A. Shakouri, L. Shi, H.-K. Lyeo and C. K. Shih, *Applied Physics Letters*, 2005, **87**, 053115.
35 K. P. Pipe, R. J. Ram and A. Shakouri, *Physical Review B*, 2002, **66**, 125316.
36 D. Alemu, H.-Y. Wei, K.-C. Ho and C.-W. Chu, *Energy & Environmental Science*, 2012, **5**, 9662.
37 J. Gasiorowski, R. Menon, K. Hingerl, M. Dachev and N. S. Sariciftci, *Thin Solid Films*, 2013, **536**, 211-215.
38 C. Liu, B. Lu, J. Yan, J. Xu, R. Yue, Z. Zhu, S. Zhou, X. Hu, Z. Zhang and P. Chen, *Synthetic Metals*, 2010, **160**, 2481-2485.
39 U. Lang, E. Müller, N. Naujoks and J. Dual, *Advanced Functional Materials*, 2009, **19**, 1215-1220.
40 S. A. Rutledge and A. S. Helmy, *Journal of Applied Physics*, 2013, **114**, 133708.
41 P. G. Karagiannidis, N. Kalfagiannis, D. Georgiou, A. Laskarakis, N. A. Hastas, C. Pitsalidis and S. Logothetidis, *Journal of Materials Chemistry*, 2012, **22**, 14624.
42 N. Koch, A. Vollmer and A. Elschner, *Applied Physics Letters*, 2007, **90**, 043512.
43 Y.-J. Lin, F.-M. Yang, C.-Y. Huang, W.-Y. Chou, J. Chang and Y.-C. Lien, *Applied Physics Letters*, 2007, **91**, 092127.
44 S. G. Im, K. K. Gleason and E. A. Olivetti, *Applied Physics Letters*, 2007, **90**, 152112.
45 R. L. Anderson, *IBM Journal of Research and Development*, 1960, **4**, 283-287.
46 D. J. Bergman and O. Levy, *Journal of Applied Physics*, 1991, **70**, 6821.
47 D. J. Bergman and L. G. Fel, *Journal of Applied Physics*, 1999, **85**, 8205.
48 R. Hull, *Properties of crystalline silicon. [electronic resource]*, London : The Institution of Electrical Engineers, c2006 (Norwood, Mass. : Books24x7.com [generator]), 2006.
49 D. J. Yun, K. Hong, S. Kim, W. M. Yun, J. Y. Jang, W. S. Kwon, C. E. Park and S. W. Rhee, *ACS applied materials & interfaces*, 2011, **3**, 43-49.
50 D. F. Mitchell, K. B. Clark, J. A. Bardwell, W. N. Lennard, G. R. Massoumi and I. V. Mitchell, *Surface and Interface Analysis*, 1994, **21**, 44-50.
51 N. Neophytou and H. Kosina, *Journal of Applied Physics*, 2012, **112**, 024305.
52 T.-G. Chen, B.-Y. Huang, E.-C. Chen, P. Yu and H.-F. Meng, *Applied Physics Letters*, 2012, **101**, 033301.
53 S. Jackle, M. Mattiza, M. Liebhaber, G. Bronstrup, M. Rommel, K. Lips and S. Christiansen, *Scientific reports*, 2015, **5**, 13008.

Figures

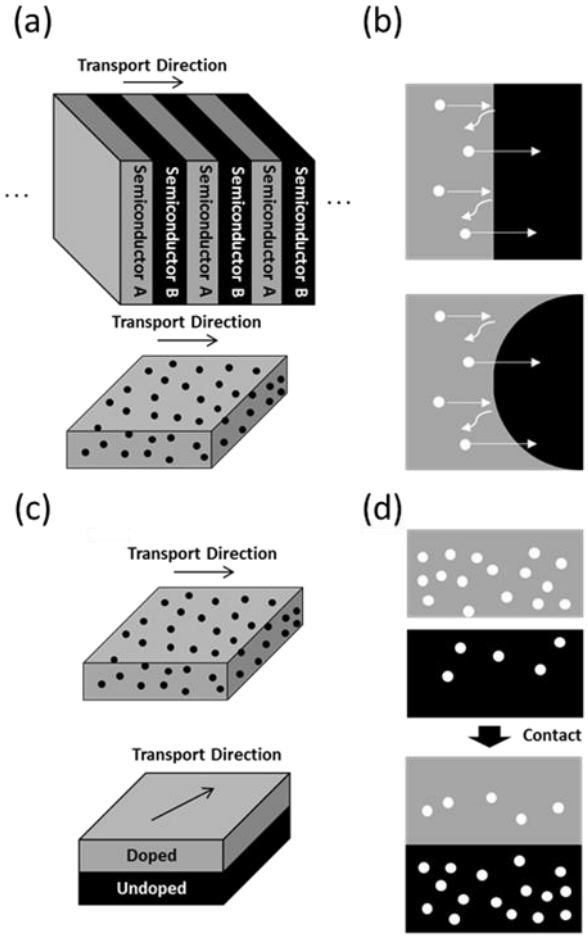

Figure 1. Schematic comparison of charge carrier scattering mechanism and modulation doping mechanism. (a) Charge carrier scattering can be an operating mechanism in composites and cross-sectional transports in superlattices. Grey slabs, black slabs, and black dots represent planar semiconductor A, planar semiconductor B, and nanostructures of semiconductor B, respectively. (b) Magnified view of the interface presented in (a). White dots represent charge carriers. (c) Modulation doping can be an operating principle for composites and planar transport of heterostructure. Grey slabs, black slab, and black dots represent planar doped semiconductor, planar undoped semiconductor, and nanostructures of undoped semiconductor, respectively (d) Magnified view of the interface presented in (d). White dots represent charge carriers.

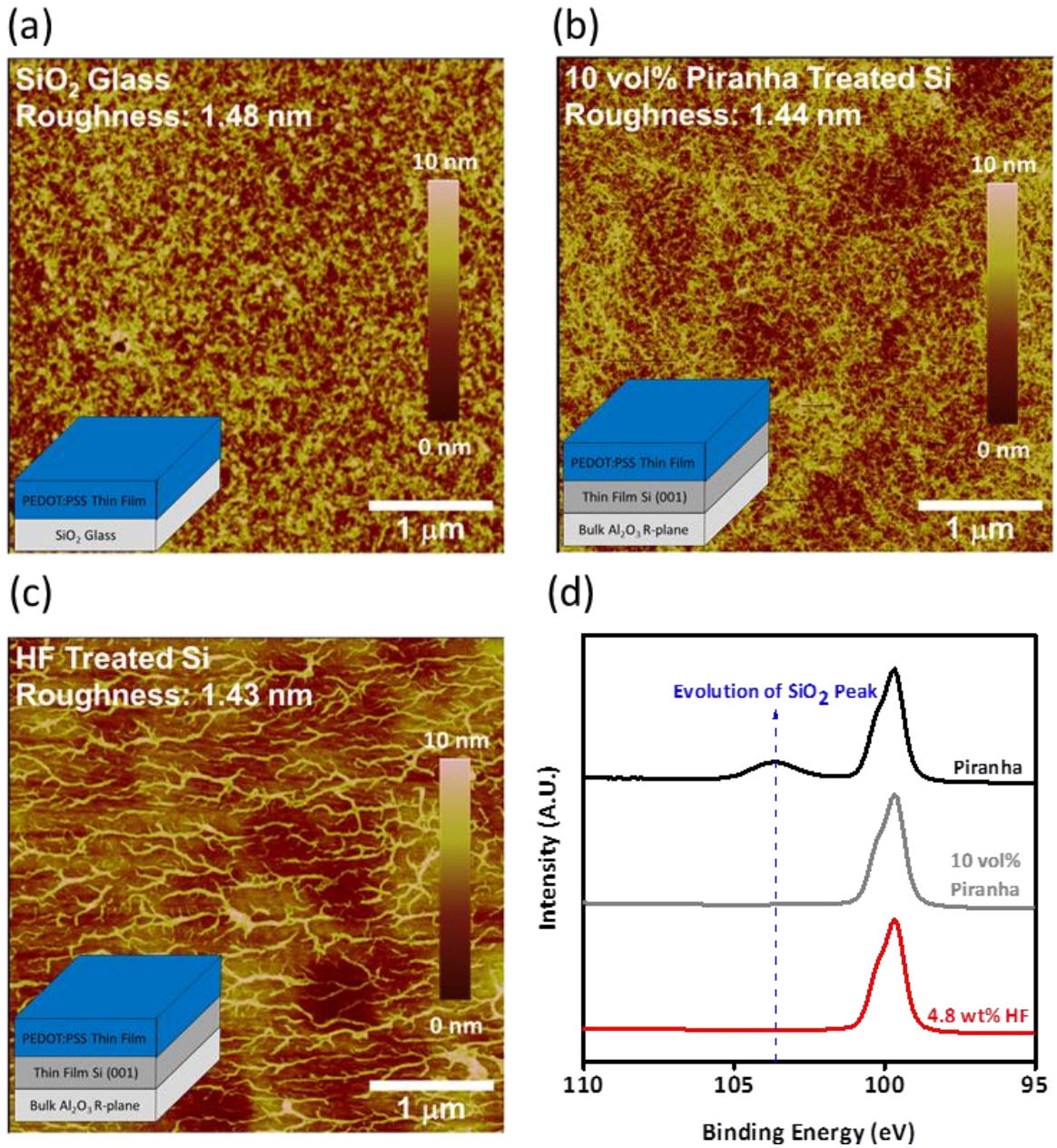

Figure 2. Morphologies of PEDOT:PSS measured by AFM. (a) PEDOT:PSS deposited on SiO_2 glass (VWR, 48366-045). (b) Morphology of PEDOT:PSS on hydrophilic Si surfaces of SOS. Si was cleaned with acetone, isopropanol and distilled water serially for 15 minutes for each step and then treated with piranha for 10 minutes. Then PEDOT:PSS was spin-coated. (c) Si was cleaned with acetone, isopropanol and distilled water serially for 15 minutes for each step and then treated with piranha for 10 minutes. SiOx was removed by 4.8 wt% HF etching for 3 minutes. Then PEDOT:PSS was spin-coated. All AFM image size is 4 × 4 μm2. (d) Si 2p XPS spectra of differently oxidized Si surfaces. As oxidation intensifies, distinct SiO_2 peaks[50] at 103.5 eV evolve more apparently, while elemental Si 2p peaks at 99.4 eV are invariant. The light black curve in the middle and red curve at the bottom underwent the same experimental procedures with (b) and (c) respectively, except for the PEDOT:PSS deposition. The black curve at the top represents Si with cleaning by acetone, isopropanol and distilled water serially for 15 minutes for each step and followed piranha treatment for 10 minutes.

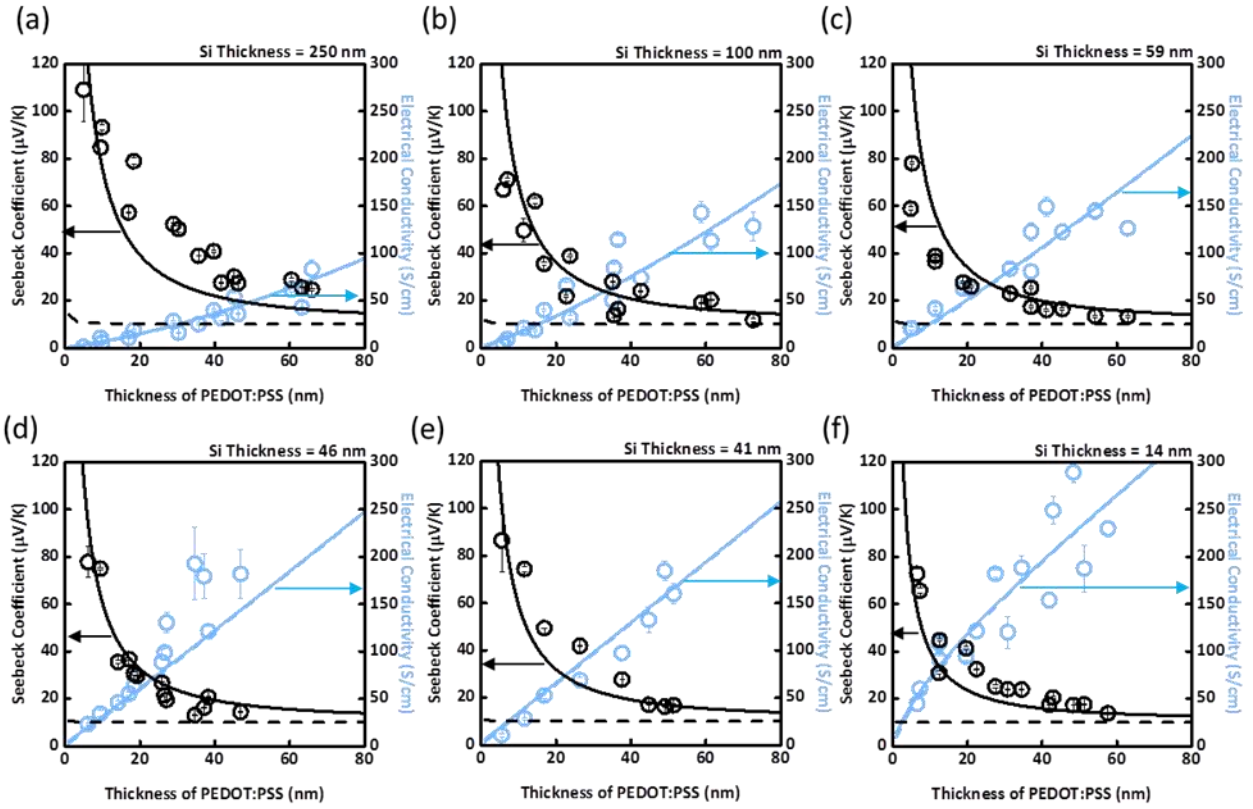

Figure 3. Experimental and Simulated electrical conductivity and Seebeck coefficient of PEDOT:PSS / Si heterostructures at different Si thicknesses as a function of PEDOT:PSS thickness. Circles represent experimental data and unbroken and dashed lines show simulation results with and without effect of band alignment, respectively. As expressed in the main text, The electrical conductivity of the heterostructure ($\bar{\sigma}$) was obtained by normalizing the sheet resistance (R) by the combined thickness of PEDOT:PSS and Si ($d_1 + d_2$), namely $\bar{\sigma} = \frac{1}{R(d_1+d_2)}$. Error bars represent the standard deviation of at least four measurements.

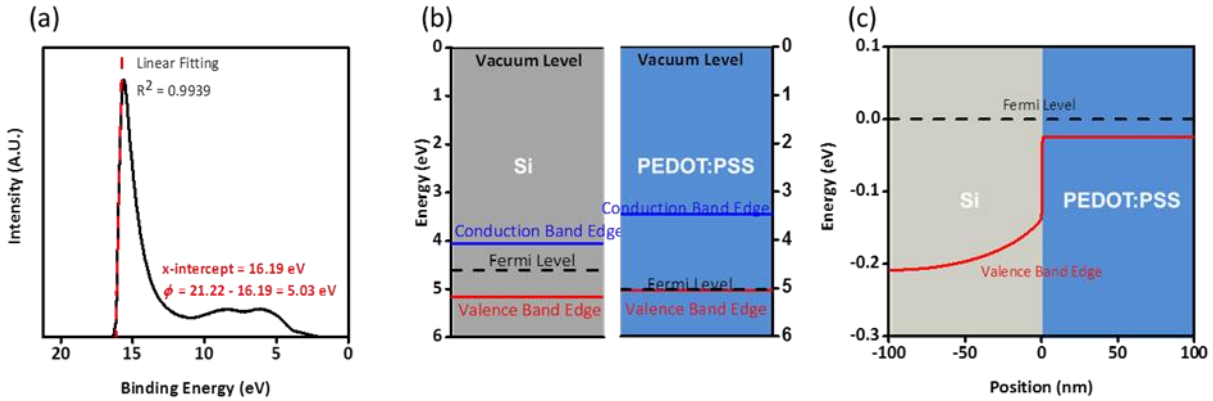

Figure 4. Band alignment of PEDOT:PSS / Si heterojunction. (a) UPS spectrum of 10 nm PEDOT:PSS on SiO_2 glass (Axis Ultra from Kratos Analytical, He I α source with 21.22 eV of energy). The x-intercept of the spectra reveals work function of PEDOT:PSS = 5.03 eV. The work function, combined with electrical conductivity of PEDOT:PSS, were adopted to simulate band alignment of PEDOT:PSS / Si heterojunction. (b) Band diagram of Si and PEDOT:PSS bands before contact to form the heterojunction. (c) Simulated valence band alignment and Fermi level of Si and PEDOT:PSS heterojunction, when Si thickness is held at 100 nm. Grey region and blue region indicate Si and PEDOT:PSS layers, respectively. Simulated such band structures for all six Si thicknesses are contained in Figure S10.

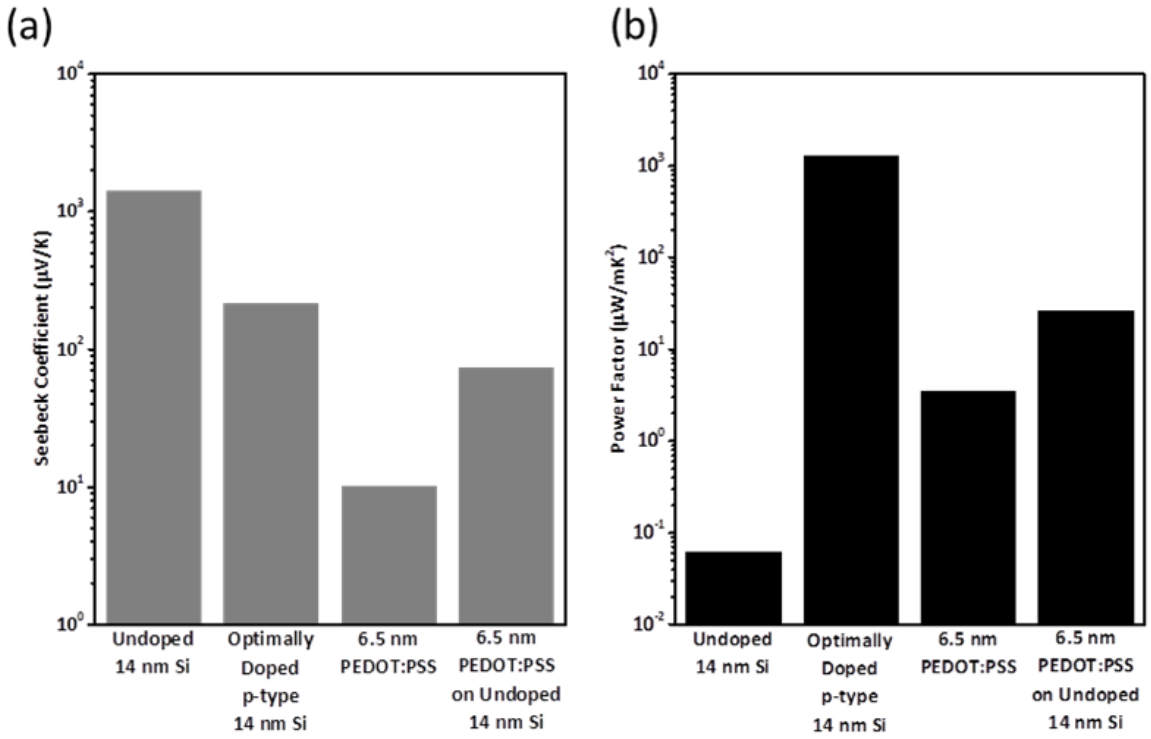

Figure 5. (a) Seebeck coefficient and (b) thermoelectric power factor comparison of 6.5-nm-thick PEDOT:PSS film on 14-nm-thick Si (100) on sapphire with respect to 6.5-nm-thick PEDOT:PSS film on SiO_2 glass slide, undoped and optimally doped[51] 14-nm-thick Si (100). These thicknesses of PEDOT:PSS and Si corresponds to the case exhibiting the largest Seebeck coefficient achieved in this study.

Table 1. Inputs for Poisson's equation

	(001) Si	PEDOT:PSS
Thickness (nm)	14 – 250	1 - 100
Band Gap (eV)	1.12 [a)]	1.57 [c)]
Work Function (eV)	4.61 [b)]	5.03
Ionization Potential (eV)	5.17 [a)]	5.05 [d)]
Acceptor Density (cm^{-3})	0	4.16×10^{20}
Valence Band Density of States (cm^{-3})	1.83×10^{19} [a)]	1.25×10^{21} [e)]
Hole Mobility ($cm^2/V{\cdot}s$)	450 [a)]	1.94 – 7.90 [f)]
Relative Dielectric Constant ($\frac{\varepsilon}{\varepsilon_0}$)	11.7 [a)]	1.1 [g)]

a) Bulk values[48]. b) Bulk electron affinity of Si and half of band gap of Si were added up, because Si was undoped[48]. c) Reported in previous study[52]. d) Difference between Fermi level and valence band maximum were taken from a previous study [53]. e) Calculated from previous study[12]. f) Dependent to thickness (see Figure S7 in the ESI†). g) Reported in previous study[37].

Graphical Abstract

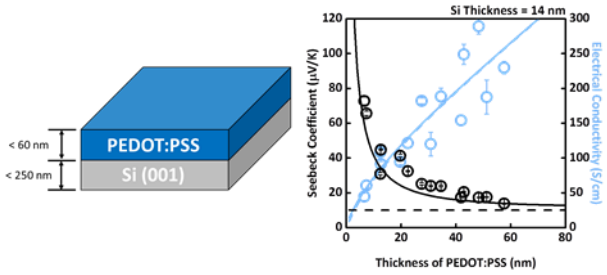

Electronic Supplementary Information

Quantitative Analyses of Enhanced Thermoelectric Properties of Modulation-Doped PEDOT:PSS / Undoped Si (001) Nanoscale Heterostructures

Dongwook Lee[a], Sayed Youssef Sayed[b, c, ‡], Sangyeop Lee[b, ‡], Chris Adam Kuryak[b], Jiawei Zhou[b], Gang Chen[b, *], and Yang Shao-Horn[a, b, c, *]

a. Department of Materials Science and Engineering, Massachusetts Institute of Technology, Cambridge, Massachusetts, United States, 02139

b. Department of Mechanical Engineering, Massachusetts Institute of Technology, Cambridge, Massachusetts, United States, 02139

c. The Research Laboratory of Electronics, Massachusetts Institute of Technology, Cambridge, Massachusetts, United States, 02139

‡ These authors contributed equally.

Sequence of Thermoelectric Performance Measurements

As PEDOT:PSS is easily damaged upon mechanical contacts, measurements with less contact with samples were conducted earlier. Hence, AFM measurement was conducted first, followed by Seebeck coefficient measurements, 4-point probe electrical conductivity measurements, and PEDOT:PSS thickness measurements.

Seebeck Coefficient Measurements[1]

The Seebeck coefficient (S) of all samples was measured with a lab-made setup. In order to determine the Seebeck coefficient, it was necessary to induce a temperature gradient across the sample and measure the voltage change (ΔV) and temperature difference (ΔT). To accomplish this, a Seebeck measurement device was built (Figure S1). The device used two commercially available Peltier modules (TE Technology, Inc.) to heat up one side of the sample and cool down the opposite side. Current was applied through the Peltier heaters in opposite directions using a current source (Keithley 2400), which made one device a heater and the other a cooler. Under each Peltier heater/cooler was a small heat sink to help conduct heat and create the largest possible temperature difference across the heater or cooler. The sample and alumina support bridged the gap between the heater and cooler.

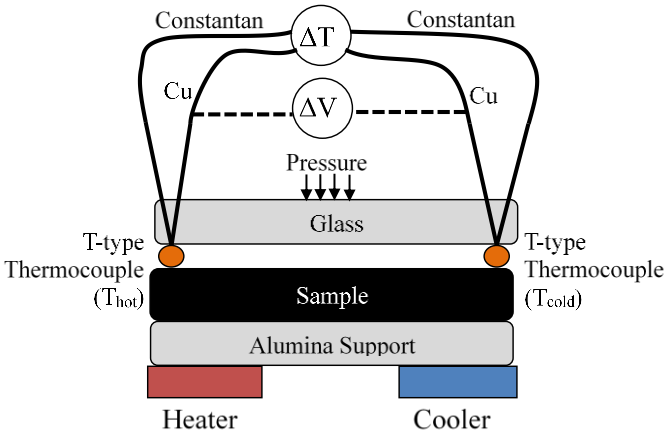

Figure S1. Schematic diagram of Seebeck coefficient measurement setup. The Peltier plates provide a temperature gradient across the sample. The temperature and voltage are measured

at the same position, by two T-type thermocouples. Pressure is provided on the thermocouples to maintain firm electrical and thermal contacts with the sample.

Electrical Conductivity Measurements by 4-point Probe and Hall Techniques

Electrical conductivity was measured by 4-point probe method (LucasLabs Pro4). To obtain a more accurate electrical conductivity measurement, 9 individual measurements were taken on each sample. These 9 measurements were averaged together to develop the reported electrical conductivity of the samples.

Hall measurements (LakeShore 7500 Series Hall System) were also adopted limitedly only to assess mobility of PEDOT:PSS film on SiO_2, as displayed at Figure S9. Those measurements yielded similar results to each other: for instance, electrical conductivity of 2.0 μm thick PEDOT:PSS on SiO_2 was 537.12 S/cm by 4-point probe measurement, and 501.88 S/cm by Hall measurement. The difference between the two measurements is less than 7 %.

PEDOT:PSS Thickness Measurements with AFM

The thickness of each sample was measured with AFM using a Veeco NanoScope IV. To obtain an estimate of the thickness, 2 lines were scratched onto the sample using a razor blade thereby exposing the substrate underneath. The step heights were measured at each of these scratches (Figure S2), and averaged values were employed as PEDOT:PSS thickness of each sample.

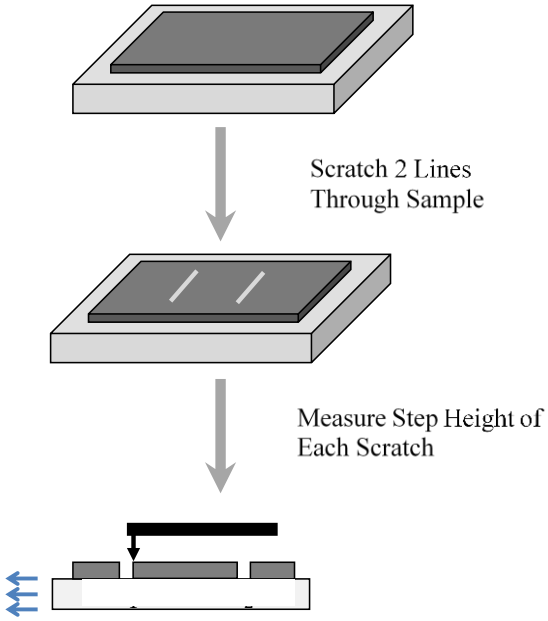

Figure S2. The procedure for thickness measurements using the AFM.

Si and SiO_x Thickness Measurements by X-ray Reflectivity (XRR)

Thickness of SiO_x layer on Si after oxide strip or generation chemical process, was examined by XRR measurements. Thickness of Si layer on sapphire after thermal oxidation and following HF etching was also determined by XRR measurements. This technique utilizes that the length of interference path depends on incident angle of the electromagnetic wave (X-ray). Therefore, the intensity of the reflected beam will have periodic rise and fall, imposed by boundary conditions, such as wavelength of the incident beam, densities and thicknesses of the films. Since the wavelength of the beam is fixed at that of Cu K α (0.15418 nm), analysis of the periodic interference pattern measured by XRR informs thickness of the thin film. Beam size was consistently 5×5 mm^2 for all XRR measurements. Figure S3 represents an exemplar XRR pattern of thermally oxidized and then HF etched SOS.

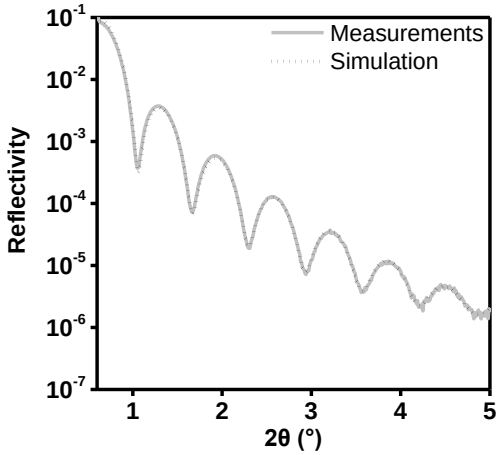

Figure S3. An exemplar interference pattern of 14 nm thick Si on sapphire measured by XRR.

Effect of Chemical Treatments on Thickness of SiO_x on SOS

SiO_x on Si is inevitable in order to accommodate PEDOT:PSS on Si surface. On the other hand, SiO_x thickness should be minimized since SiO_x can complicate analysis and modelling for numerical simulation. Exposing the etched surface to 10 vol% piranha satisfies those two conflicting requirements by creating a hydrophilic surface to deposit PEDOT:PSS (Figure 1c), as well as generating sub-nanometer thick SiO_x layer (Figure S4).

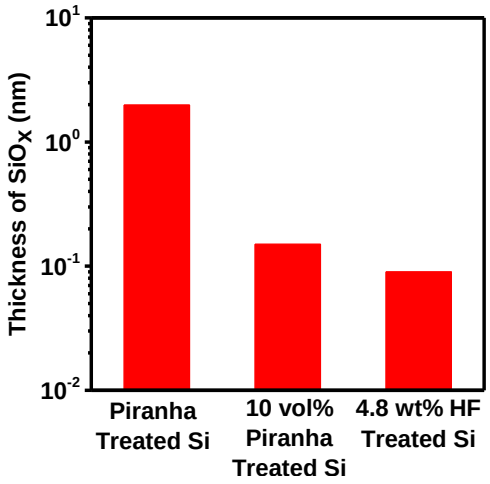

Figure S4. Thicknesses of SiO_x on Si by varying chemical treatments on SOS wafers, measured with XRR.

Thermal Oxidation of SOS for Silicon Thickness Control

Thermal oxidation of SOS was introduced in order to decrease the thickness of the Si layer. It converts Si into SiO_2 from the interface with air at certain rate under specific temperature, humidity, and crystalline orientation[2]. SiO_x was removed after thermal oxidation with HF etching.

Before thermal oxidation RCA 1 and RCA 2 cleaning procedures were conducted in order to minimize the introduction of metallic elements to Si[2], which could turn into dopants after thermal oxidation. For this study, we used dry oxidation at 1100 ^oC for varying time duration for (001) SOS under 40 mL/s of dry oxygen flow, as high temperature at 1100 ^oC ensures quick oxidation, and dry condition tend to produce atomically flat surface[2]. Figure S5 shows morphology of the resultant SOS after thermal oxidation, and resultant resistivity of thinned down SOS. The thermal growth of SiO_2 layer followed established empirical trend[2], which is summarized at Figure S6.

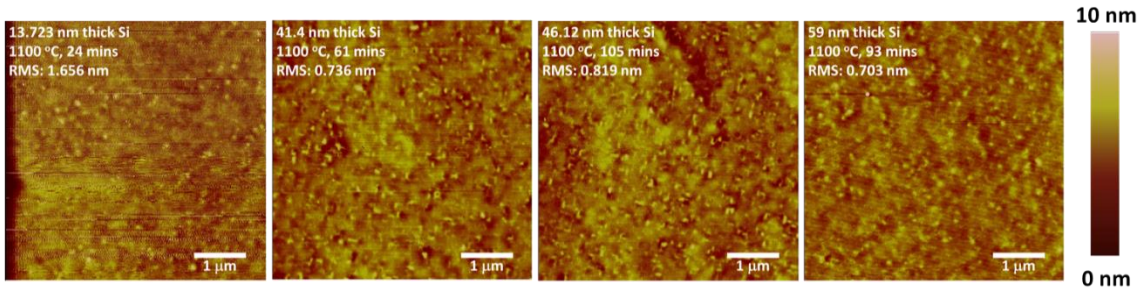

Figure S5. Surface roughnesses of Si were kept flat even after thermal oxidation at 1100 ^oC for varying durations, and following HF removal of thermally grown SiO_x.

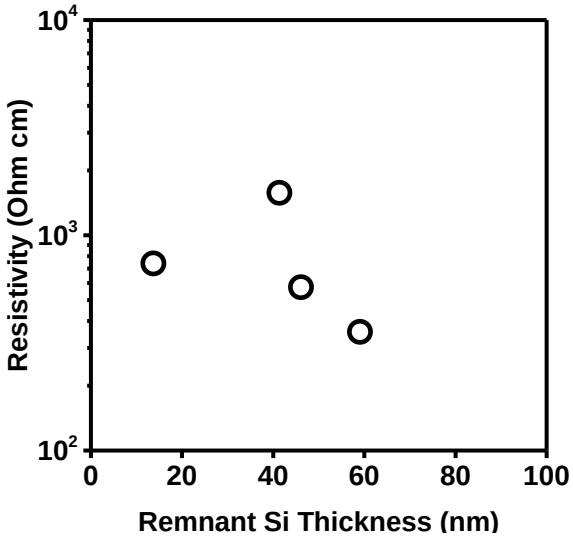

Figure S6. Resultant resistivity of SOS after thermal oxidation and subsequent HF etching. Resistivity remained highly intrinsic even after the thermal oxidation.

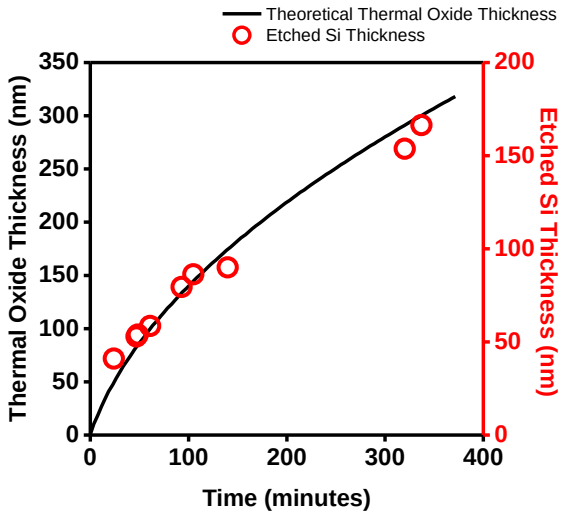

Figure S7. Thermal growth of SiO_2 on (001) Si shows agreement with theoretical Deal-Grove model, where oxygen gas diffuses from the outside to the surface, then through the existing oxide layer to the oxide-substrate interface, and then lastly reacts with buried Si atoms[2].

Dependence of Sheet Resistance on Combined Thickness of PEDOT:PSS and Si

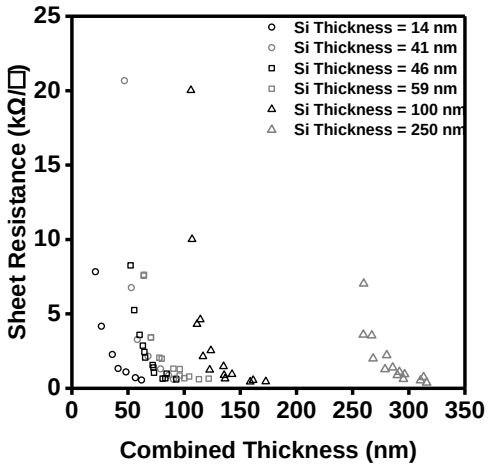

Figure S8. Sheet resistances of PEDOT:PSS / Si heterostructure. The sheet resistance mainly depends on PEDOT:PSS thickness, not Si thickness. Almost identical trends are shifted horizontally due to different Si thicknesses. Black circles, grey circles, black squares, grey squares, black triangles, and grey triangles correspond to 14 nm, 41 nm, 46 nm, 59 nm, 100 nm, and 250 nm of Si thicknesses, respectively.

Evolution of Electrical Conductivity and Mobility of PEDOT:PSS on SiO_2 Quartz by Variation of Thickness

Thickness dependence of electrical conductivity of thin films on insulating substrate is a general phenomenon for various materials[3-5]. Especially for PEDOT:PSS thin films on various insulating substrates, increase in film thickness accompanies increase in film thickness[6, 7]. Measured electrical conductivity of PEDOT:PSS on SiO_2 quartz substrate shares the similar trends for investigated range of thickness (5 – 60 nm), as shown in Figure S9. It should be noted that linear fitting of PEDOT:PSS electrical conductivity evolution does not have theoretical basis so far. This linear fitting was adopted only to provide an estimation of PEDOT:PSS electrical conductivity trend within the researched thickness region in this study.

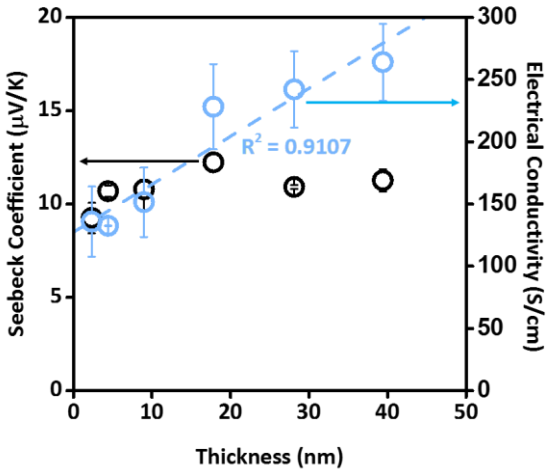

Figure S9. Electrical conductivity of PEDOT:PSS on SiO_2 quartz with linear fitting. Note that linear trend does not have theoretical justification. Seebeck coefficient of PEDOT:PSS on SiO_2 quartz is constant, which evidences hole density of PEDOT:PSS is invariant.

Distinguishing mobility and hole density from electrical conductivity is necessary to solve Poisson's equation. However, it has been widely reported that low mobility of PEDOT:PSS[8, 9] renders Hall measurement technically difficult[10]. Only for PEDOT:PSS on SiO_2 with micron-scale thickness (6.78 μm), linear relation between Hall voltage and applied external magnetic field could be found, as shown in Figure S10. PEDOT:PSS with less thickness failed to produce clear linear relation, therefore mobility and hole density could not be measured for that range of thickness. Mobility and hole density could be obtained by following formulas, as indicated below, where $n, \mu, \sigma, e, d,$ and a represent hole density, mobility, electrical conductivity, elementary charge, thickness of PEDOT:PSS, and slope of Figure S10.

$$n = \frac{1}{aed} \tag{S1}$$

$$\mu = \frac{\sigma}{ne} \tag{S2}$$

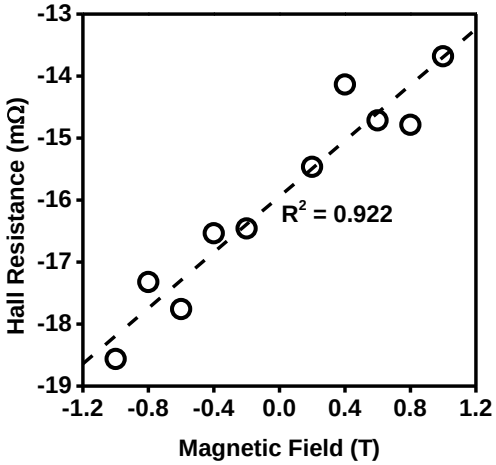

Figure S10. Hall resistance showed a linear relationship with applied external magnetic field, only when thickness of PEDOT:PSS on SiO_2 was in micrometer range. For PEDOT:PSS with nanometer scale thickness, trends were completely noisy.

Therefore, it could be concluded that mobility and hole density of 6.78 μm thick PEDOT:PSS are 7.90 $cm^2/V{\cdot}s$ and 4.16×10^{20} cm^{-3}, respectively. The measured hole density of PEDOT:PSS is at similar range with previously reported values[11].

Even though direct measurement of hole density was not possible for PEDOT:PSS with less than μm scale, it was still possible to draw hole density from Seebeck coefficient measurement. Seebeck coefficient of PEDOT:PSS strictly is only affected by hole density, as reported in a previous research[7, 12].

Combined with constant Seebeck coefficient trend of PEDOT:PSS at Figure S9, it can be concluded that hole density of PEDOT:PSS stays the same as well. Given that electrical conductivity of PEDOT:PSS depends on thickness, then it is mobility that varies with thickness. This result was employed as input parameters for Poisson's equation.

Band Alignment of PEDOT:PSS Thin Film on Si with Varying Thicknesses

The numerical simulation of Poisson's equation by COMSOL Multiphysics® Modeling Software analyzed band bending at equilibrium after the heterojunction formation, for various thicknesses of (001) Si (Figure S11). Band bending does not happen at PEDOT:PSS layer, as PEDOT:PSS has nearly metallic hole density. At the Si side close to the interface, the band offset and band bending is preserved regardless of Si thicknesses. This implies no significant change in Seebeck coefficient trend, since the contribution to Seebeck coefficient from the region far from the interface is negligible, as explained in the main text.

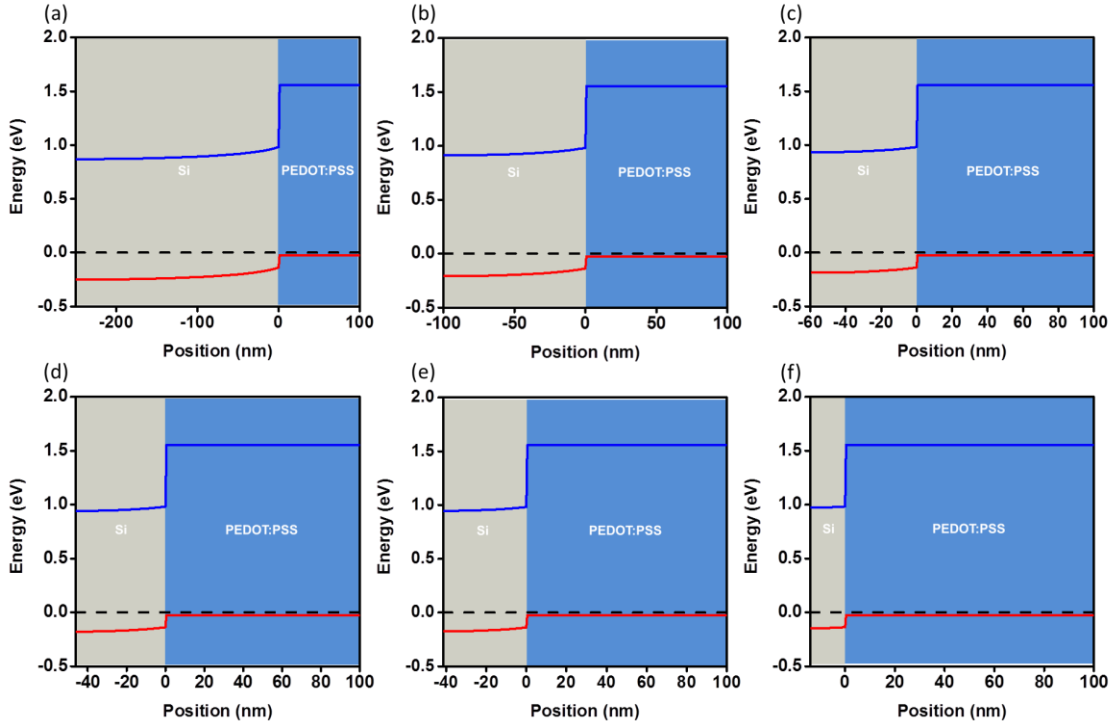

Figure S11. (a) – (f) Band diagrams of PEDOT:PSS / Si heterojunction at 250 nm, 100 nm, 59 nm, 46 nm, 41 nm, and 14 nm thick Si.

Modeling of the Seebeck Coefficient and Electrical Conductivity: without Band Bending

As explained in the main text, parallel resistor model was assumed to estimate theoretical Seebeck coefficient and electrical conductivity. When no band bending upon contact between PEDOT:PSS and Si is assumed, charge distribution within PEDOT:PSS and Si will be unchanged. This means Seebeck coefficient and electrical conductivity of PEDOT:PSS and Si will stay the same. Therefore, theoretical Seebeck coefficient and electrical conductivity of PEDOT:PSS / Si heterostructure can be expressed by following formalism:

$$\frac{1}{\bar{R}} = \frac{1}{R_1} + \frac{1}{R_2} \quad \text{(S3)}$$

$$\bar{\sigma}(d_1 + d_2)\frac{w}{l} = \sigma_1 d_1 \frac{w}{l} + \sigma_2 d_2 \frac{w}{l} \quad \text{(S4)}$$

$$\boldsymbol{\bar{\sigma} = \frac{\sigma_1 d_1 + \sigma_2 d_2}{d_1 + d_2}} \quad \textbf{(S5)}$$

$$\frac{\bar{S}}{\bar{R}} = \frac{S_1}{R_1} + \frac{S_2}{R_2} \quad \text{(S6)}$$

$$\bar{\sigma}\bar{S}(d_1 + d_2)\frac{w}{l} = \sigma_1 S_1 d_1 \frac{w}{l} + \sigma_2 S_2 d_2 \frac{w}{l} \quad \text{(S7)}$$

$$\boldsymbol{\bar{S} = \frac{S_1 \sigma_1 d_1 + S_2 \sigma_2 d_2}{\sigma_1 d_1 + \sigma_2 d_2}} \quad \textbf{(S8)}$$

where R_1, R_2, d_1, d_2, σ_1, σ_2, S_1, and S_2 represent resistance, thickness, electrical conductivity, and Seebeck coefficient of Si and PEDOT:PSS respectively. w and l mean width and length of the sample, which always were 1.0 cm. $\bar{\sigma}$ and $\bar{S}$ are electrical conductivity and Seebeck coefficient of PEDOT:PSS / Si heterostructure.

Modeling of the Seebeck Coefficient and Electrical Conductivity with Band Bending

When band bending is assumed, valence band edge at each position changes, as shown in Figure S11. The band bending causes different hole density at each position. Therefore hole

density at certain position can be converted to electrical conductivity and Seebeck coefficient at corresponding position. Charge scattering mechanism in PEDOT:PSS and Si were regarded the same even after modulation doping, leading to preserved mobility of holes in Si and PEDOT:PSS. Pisarenko relation of PEDOT:PSS[12] and (001) Si[13-16] at room temperature were adopted to evaluate Seebeck coefficient at specific hole density. Detailed mathematical expressions are shown below:

$$\sigma_1(n_1(x)) = n_1(x)e\mu_1 \quad \text{(S9)}$$

$$\sigma_2(n_2(x)) = n_2(x)e\mu_2 \quad \text{(S10)}$$

$$S_1(n_1(x)) = \frac{k_B}{e}\left(\ln\left(\frac{N_{V1}}{n_1(x)}\right) + 3\right) \text{ at room temperature} \quad \text{(S11)}$$

where μ_1 and μ_2 are the mobility of holes in Si and PEDOT:PSS layer, N_{V1} the valence band density of states of Si, k_B the Boltzmann constant, e the elementary charge, respectively. Hole density dependent Seebeck coefficient of PEDOT:PSS, $S_2\left(n_2(x)\right)$, was taken from Pisarenko plot in the previous research[12].

In order to evaluate the overall sample thermoelectric properties, averaging the Seebeck coefficient and electrical conductivity over the entire thickness of PEDOT:PSS and Si were needed. Parallel resistor model was applied and each position was regarded as a resistor. Detailed mathematical expressions are shown below.

$$\frac{1}{\bar{R}} = \sum_i \frac{1}{R_i} \quad \text{(S12)}$$

$$\bar{\sigma} = \frac{\int_{-d_1}^{0} n_1(x)e\mu_1 dx + \int_0^{d_2} n_2(x)e\mu_2 dx}{d_1+d_2} \quad \text{(S13)}$$

$$\bar{S} = \frac{\int_{-d_1}^{0} S_1(x)n_1(x)e\mu_1 dx + \int_0^{d_2} S_2(x)n_2(x)e\mu_2 dx}{\bar{\sigma}(d_1+d_2)} \quad \text{(S14)}$$

where R_i is resistance of individual infinitesimal resistors, $\bar{R}$, $\bar{\sigma}$, and $\bar{S}$ represent resistance, thickness, electrical conductivity, and Seebeck coefficient of overall samples, respectively.

Power Factors at Various Si Thicknesses

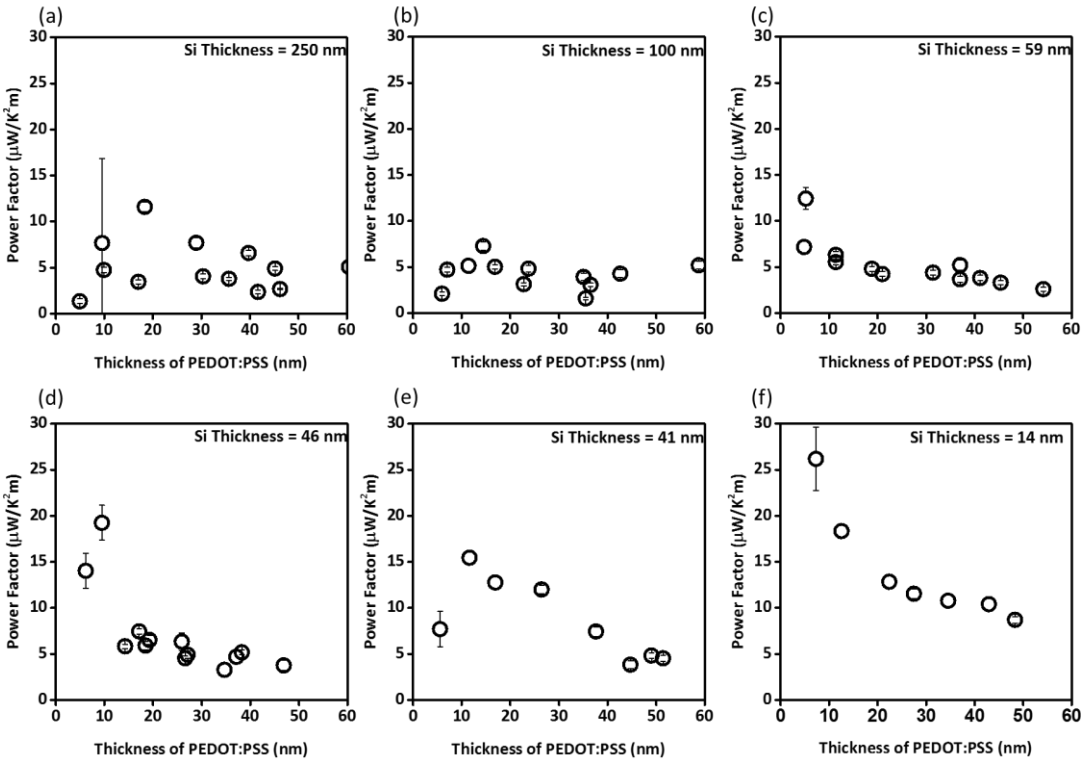

Figure S12. (a) – (f) Power factors of PEDOT:PSS films of different thicknesses on 250 nm, 100 nm, 59 nm, 46 nm, 41 nm, and 14 nm thick Si, respectively. These are estimated from multiplying individually measured Seebeck coefficients and electrical conductivities.

Power Factors at Various Combined Si and PEDOT:PSS Thicknesses

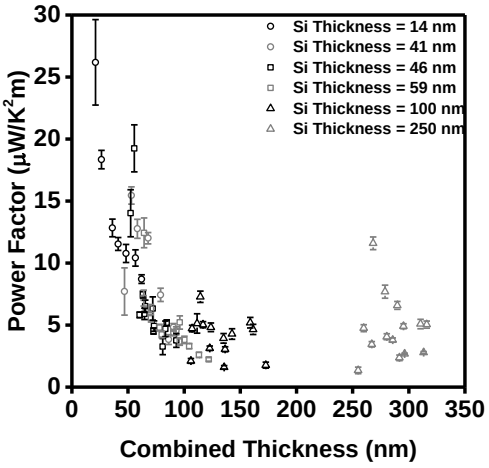

Figure S13. Power factors of PEDOT:PSS / Si heterostructure consistently increases as combined thickness of the heterostructure decreases. Decreasing Si thickness improves electrical conductivity by reducing portion of undoped Si far from the interface for electrical conductivity normalization. Reducing PEDOT:PSS thickness sacrifices electrical conductivity, while Seebeck coefficient increases. Those trends are reflected in this plot. Black circles, grey circles, black squares, grey squares, black triangles, and grey triangles correspond to 14 nm, 41 nm, 46 nm, 59 nm, 100 nm, and 250 nm of Si thicknesses, respectively.

UV – Vis - NIR Spectra of 6.5 nm PEDOT:PSS, 14 nm SOS, and 6.5 nm PEDOT:PSS on 14 nm SOS

It has been known that when PEDOT:PSS undergoes doping / dedoping by chemical treatments, such as application of solvents, its transmission pattern changes, as dominant transitions between its subbands alters their probabilities[12]. UV – Vis – NIR was employed to determine if 6.5 nm thick PEDOT:PSS on 14 nm thick SOS and bulk SiO_2 exhibits different doping state (Figure S14). Because the absorption is mostly governed by SOS, it is not possible to clarify PEDOT:PSS doping state dependence on substrates.

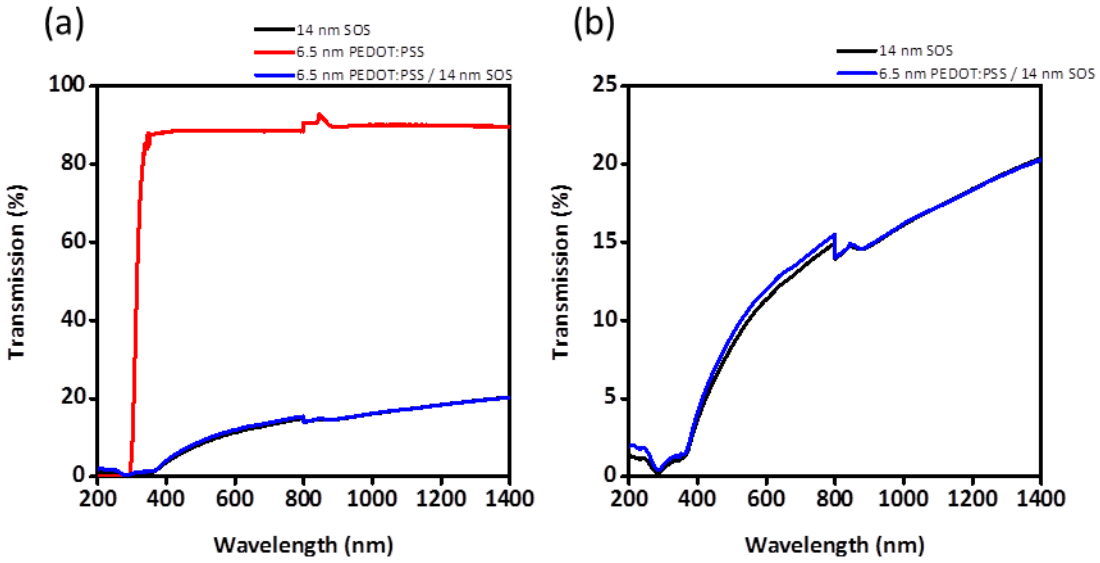

Figure S14. Transmission spectra at UV-Vis-NIR wavelength region of 14 nm thick SOS, 6.5 nm thick PEDOT:PSS on bulk SiO_2, and 6.5 nm thick PEDOT:PSS on 14 nm thick SOS.

Preferred Orientation of PEDOT:PSS

It is very plausible for PEDOT:PSS thin film on Si and SiO_2 to have preferred orientations. Adoption of co-solvents, such as ethanol and DMSO so far proved effective to align nanoscale grains of PEDOT favorable for hole conduction[17-19], as it realigns to enhance hole hopping rate from PEDOT nanograin to another[17], thereby improving mobility of holes in PEDOT:PSS. This is another reason why we also adopted mixture of PEDOT:PSS with co-solvents of ethanol and DMSO, in addition to wettability issue on Si surface.

References

1. C. A. Kuryak, *Nanostructured thin film thermoelectric composite materials using conductive polymer PEDOT:PSS*, c2013., 2013.
2. G. E. McGuire, *Semiconductor materials and process technology handbook : for very large scale integration (VLSI) and ultra large scale integration (ULSI)*, Park Ridge, N.J., U.S.A. : Noyes Publications, c1988., 1988.
3. N. Yoshikatsu, *Japanese Journal of Applied Physics*, 1970, **9**, 1326.
4. A. F. Mayadas and M. Shatzkes, *Physical Review B*, 1970, **1**, 1382-1389.
5. K. Fuchs, *Mathematical Proceedings of the Cambridge Philosophical Society*, 1938, **34**, 100-108.
6. W. Seifert, H. Albrecht, S. Mietke, T. Kohler and M. Werner, Place of Publication: San Diego, CA, USA. Country of Publication: USA.
7. D. Yoo, W. Son, S. Kim, J. J. Lee, S. H. Lee, H. H. Choi and J. H. Kim, *RSC Advances*, 2014, **4**, 58924-58929.
8. S. A. Rutledge and A. S. Helmy, *Journal of Applied Physics*, 2013, **114**, 133708.
9. R. Coehoorn, W. F. Pasveer, P. A. Bobbert and M. A. J. Michels, *Physical Review B*, 2005, **72**.
10. L. A. Eldada, J. Lindemuth and S.-I. Mizuta, 2011, **8110**, 81100I.
11. C. Liu, B. Lu, J. Yan, J. Xu, R. Yue, Z. Zhu, S. Zhou, X. Hu, Z. Zhang and P. Chen, *Synthetic Metals*, 2010, **160**, 2481-2485.
12. O. Bubnova, M. Berggren and X. Crispin, *Journal of the American Chemical Society*, 2012, **134**, 16456-16459.
13. Z. Bian, A. Shakouri, L. Shi, H.-K. Lyeo and C. K. Shih, *Applied Physics Letters*, 2005, **87**, 053115.
14. H.-K. Lyeo, A. A. Khajetoorians, L. Shi, K. P. Pipe, R. J. Ram, A. Shakouri and C. K. Shih, *Science*, 2004, **303**, 816-818.
15. K. P. Pipe, R. J. Ram and A. Shakouri, *Physical Review B*, 2002, **66**, 125316.
16. B. Lee, K. Kim, S. Lee, J. H. Kim, D. S. Lim, O. Kwon and J. S. Lee, *Nano Lett*, 2012, **12**, 4472-4476.
17. Y. Xia and J. Ouyang, *Journal of Materials Chemistry*, 2011, **21**, 4927-4936.
18. J. P. Thomas and K. T. Leung, *Journal of Materials Chemistry A*, 2016, DOI: 10.1039/c6ta07410c.
19. E. Jin Bae, Y. Hun Kang, K.-S. Jang and S. Yun Cho, *Scientific reports*, 2016, **6**, 18805.